Evolving Material Porosity on an Additive Manufacturing Simulation with the Generalized Method of Cells

Luis F. Silva[1] and Francisco Yapor[2]
Western Michigan University, Kalamazoo, MI, 49008, USA

Evan J. Pineda[3]
NASA Glenn Research Center, Cleveland, OH, 44135, USA

Peter A. Gustafson[4]
Western Michigan University, Kalamazoo, MI, 49008, USA

The effect of material porosity on final part distortion and residual stresses in a selective laser sintering manufacturing simulation is presented here. A time-dependent thermo-mechanical model is used with the open-source FEA software CalculiX. Effective homogenized material properties for Inconel 625 are precomputed using NASA's Micromechanics Analysis Code with Generalized Method of Cells (MAC/GMC). The evolving porosity of the material is estimated with each pass of the laser beam during simulation runtime. A comparison with a homogenous model and the evolving model shows that the evolving porous model predicts larger distortions with greater residual stresses.

I. Nomenclature

ε	=	sintered porosity
ε_0	=	initial porosity
$\varepsilon_{\min}$	=	minimum achievable porosity
K	=	densification coefficient
V_f	=	volume fraction
s	=	laser beam penetration depth
η	=	laser power transmission efficiency
r_0	=	laser beam radius
v	=	laser linear speed
l, w	=	length and width of the laser scan area
ψ	=	specific energy input
P	=	nominal laser power
υ	=	Poisson's ratio
E	=	modulus of elasticity
S, S_y	=	stress, yield stress

[1] MS Candidate, Mechanical and Aerospace Engineering.
[2] PhD Candidate, Mechanical and Aerospace Engineering, and AIAA Member
[3] Aerospace Research Engineer, Multiscale and Multiphysics Modeling Branch, and AIAA Senior Member
[4] Associate Professor, Mechanical and Aerospace Engineering, and AIAA Member

ε_p	=	plastic strain
ρ	=	mass density
k	=	thermal conductivity
h	=	convective heat transfer coefficient
C	=	specific heat capacity
α	=	coefficient of thermal expansion
T	=	Temperature

II. Introduction

Advancements in additive manufacturing (AM) have made it a viable solution for the rapid prototyping and manufacturing of geometrically complex structures. However, the associated part deformation may cause unacceptable dimensional deviations, and the accompanying residual stresses can cause premature failure or otherwise weaken the overall structure. These residual stresses occur primarily due to large temperature gradients in AM processes such as selective laser sintering (SLS) [1]. Prediction of these residual fields, optimization of the part and the manufacturing process are desirable.

AM with SLS uses a high-powered laser to selectively fuse a metal powder bed, a single layer at a time, into a fully formed part. It is this process of localized material heating and subsequent cooling that induces residual stresses [1]. Previous literature has indicated that these stresses are linked to a variety of process parameters, including layer thickness and laser beam characteristics [2].

Previous physical modeling of the SLS thermo-mechanical process include finite element (FE) methods, where a transient thermo-mechanical model is solved [3]. However, there have been disagreements between these models and experimental results, even after mesh refinements and temperature-dependent material properties [3]. Typically, these FE simulations model the material as a homogenous material. Discrete element methods have also been used to account for the heterogeneous nature of the metal powder, simulating an individual or a group of particles and their thermo-mechanical behavior. However, the discrete element method suffers from large computational time requirements [3].

The generalized method of cells (GMC) uses a repeating unit cell (RUC) to represent the microstructural domain of a material. Each RUC then contains sub-cells that are representative of distinct phases or distinct materials in a composite, or in this case, neighboring metal particles and trapped air in the powder during the sintering process. The material properties and dimensions of each sub-cell can then be used to compute the effective homogenized macroscopic response (stress/strain, thermal/mechanical material properties) of the RUC through enforcing traction and displacement continuity conditions [4]. These effective material properties are used in the constitutive model for the FE simulation, effectively cascading the microstructural response onto the macroscale. GMC can incorporate complex, multi-scaled nonlinear material analysis. The RUC has the advantage that it can capture the gradients at the microscale, as opposed to other microstructural to macrostructural estimates, such as the Voigt approximation or the Reuss approximation [4, p. 105].

This manuscript estimates the effect of the material porosity on residual stresses and residual distortions during the process simulation. The evolving porosity of the material is estimated at runtime and used to calculate the effective homogenous material properties using GMC. The properties are then tabulated dependent on temperature and porosity for use during runtime of a time-dependent thermo-mechanical FE simulation. The effect of the decreasing material porosity from powder to solid is shown to affect the residual stress and deformation fields.

III. Methodology

A. Thermomechanical FE Simulation

The additive manufacturing process was simulated using a thermo-mechanical FE model. In this model a transient heat transfer problem is solved for temperature; then, the distribution is applied as a temperature change to a quasistatic structural simulation at every time step. The nonlinearity from temperature-dependent material properties, the temperature-dependent plasticity model, radiation effects in the thermal model, and the changing materials from powder to solid require an iterative solution at every time step. Modeling of liquid phases, the latent heat of a solid to liquid phase change, and any creep effects are neglected. The open-source FE software CalculiX was used to perform the simulations.

External thermal loading was accomplished through a user-defined subroutine in CalculiX. This allows for controlled laser properties such as its path, intensity, and applied heat flux distribution. It has been shown that the

laser scanning pattern influences the residual stresses of the final part [5]. Thus, the open-source 3D slicer software, Slic3r, was used to generate g-code describing the laser path of the part. The laser path produced by Slic3r is intended for a fused deposition modeling (FDM) 3D printing process. It was deemed the path produced was appropriate for this application. The software can be configured with various laser scanning strategies.

A script was written to parse the g-code. It estimates the time required to perform each g-code operation from the laser speed. The script then interpolates the position of the laser at regular time intervals to populate a tabulated file. This file was then read by the user-defined subroutine (DFLUX) during the runtime in CalculiX.

The user subroutine applies a Gaussian distributed volumetric heat flux Q as computed by Eq. (1) from Ref. [6] to the corresponding integration points, at the current simulation time, simulating the laser energy input [7]. Note that, the expression $\pi\left(1-\exp\left(K_z s\right)\right)$ is constant in this model at approximately -59.959. The variables x and y are the distances from the beam's center in the respective directions to the integration point, and z is the distance from the top surface to the integration point.

$$Q(x,y,z) = \frac{kK_z \eta P}{\pi\left(1-\exp\left(K_z s\right)\right)} \exp\left(-kr^2 - K_z z\right)$$
$$r^2 = x^2 + y^2 \tag{1}$$
$$K_z = 3/s$$
$$k = 3/r_0^2$$

Element activation simulates the addition of material deposited at every layer. A deactivated element is not computed as part of the solver pass. Each layer of elements represents several layers of the AM process, as the thickness of an FE element is substantially larger than the thickness of a powder layer. Previous FE simulations in literature as in Ref. [8] have used a couple of elements through the thickness to represent several AM layers. A new layer of elements is added after the laser has finished passing through the previous layer. During the activation, since the layer below the newly added elements has already been strained, artificial strain is added to the newly activated elements. This ensures that the newly added, yet deformed element is stress-free. This is the default action by CalculiX.

Another python script performs the sectioning of a predetermined FE mesh into sets of element layers. After reading the input mesh file, the script categorizes each element into a layer and then appends the element list to the input file. For implementation, the *STEP keyword was used in the input deck with the *MODEL CHANGE keyword to perform the addition of the layers. Thus, the input deck is read once, while the laser information and material data (discussed in the next section) are read at every iteration. Fig. 1 shows the overall flowchart of the implementation.

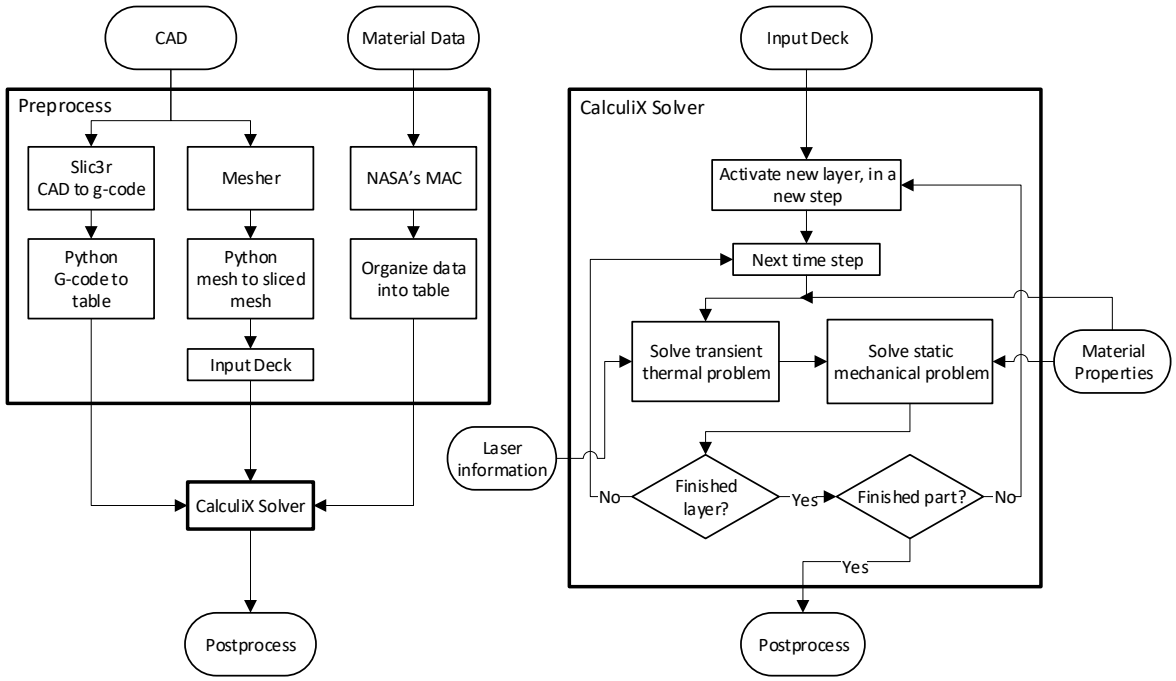

Fig. 1 Implementation flowchart

At a given time step, each layer of elements contains sintered and powdered material. The distinction is made by the material properties of the integration point. A layer is initialized with powered material properties. During runtime sintered material properties are assigned once the laser has passed over the integration point.

Locally, mechanical loading is a result of the thermal expansion as calculated in the thermal simulation. The mechanical simulation uses incremental pointwise plasticity as the material constitutive law, assuming isotropic hardening. This was implemented within the user material subroutine by a call to the incremental plasticity subroutine native to CalculiX.

B. Material Properties

Internal, solution-dependent state variables were used to track the physical state of the material microstructure. Solution-dependent state variables in CalculiX exist for each integration point in the model. Thus, a single element can have different material properties at each of the integration points in a simulation. One solution-dependent state variable is used to store the current predicted porosity of the material and another to differentiate powder from sintered material. For visualization purposes, a third was used to store the current structural elastic modulus of the material.

CalculiX sources were modified to allow for a thermal and structural user material capable of altering material properties as determined by interpolating the material properties in a lookup table. This predetermined table of material properties tabulated the material constitutive relationship (elastic modulus, Poisson's ratio, and plastic strain/stress pairs), thermal conductivity, specific heat, and thermal expansion coefficients as a function of temperature, material state (powder or solid) and volume fraction of air to solid (porosity) of the sintered material. This was accomplished by modifying the "materialdata_me.f" and "materialdata_th.f" subroutines in CalculiX to read the properties from the tabulated file and perform a 2D interpolation of the table (once for temperature and again for porosity). If the temperature or porosity being requested is out of bounds from the values specified in the table, the closest temperature or porosity in the table is used (no extrapolations).

The evolution of the porosity of the sintered material ε is predicted during runtime from Eq. (2) obtained from Ref. [9], where ε_0 is the initial porosity of the powder (assumed here to be 0.3), and $\varepsilon_{\min}$ is the minimum attainable porosity (assumed here to be 0.0001). The assumptions for the initial and minimum values of porosity are preliminary, used to establish the method. In the future, these properties will be measured. Note that, the densification coefficient K is a function of powder diameter, distribution, and material properties [9]. Here, it was assumed to be constant at 18.97 $\mathrm{mm}^3/\mathrm{kJ}$.

The specific energy input ψ is calculated using the laser power P_z, laser linear velocity v, and the laser scan area, characterized by l and w, as shown in Eq. (4). The product lw is taken as πr_0^2. The volume fraction V_f of the sintered material is taken as $V_f = 1 - \varepsilon$. The laser penetration was assumed to exponentially decay into the material as shown in Eq. (5), K_z is as defined in Eq. (1). It was also assumed that, the estimated porosity ε for an already sintered layer (the layers below the topmost layer) can be used as the initial porosity ε_0 in Eq. (3) for subsequent passes of the laser, at each time step. Thus, the porosity of all the layers in the model change during the simulation.

$$\ln(1-D) = -K\psi \tag{2}$$

$$D = \frac{\varepsilon - \varepsilon_0}{\varepsilon_{\min} - \varepsilon_0} \tag{3}$$

$$\psi = \frac{P_z}{vlw} \tag{4}$$

$$P_z = \eta P \exp(-K_z z) \tag{5}$$

The macroscopic homogenized material properties were precomputed using NASA's Micromechanical Analysis Code – Generalized Method of Cells (MAC-GMC). A triply periodic open-cell RUC was chosen for the representative arrangement of the partially sintered material, as shown in Fig. 2. In the figure, a dark blue rectangular subcell represents a solid material, and a translucent blue represents air. Note that this RUC is assumed to be isotropic, thus no need to store any anisotropic material properties.

The linear version of GMC (used here) calculates the material properties on an average sense [4]. That is, the stress carried by the RUC in a direction is evenly carried across the subcells. Stress concentrations due to corners are not resolved. Thus, a spherical representation would effectively be seen as a rectangular subcell.

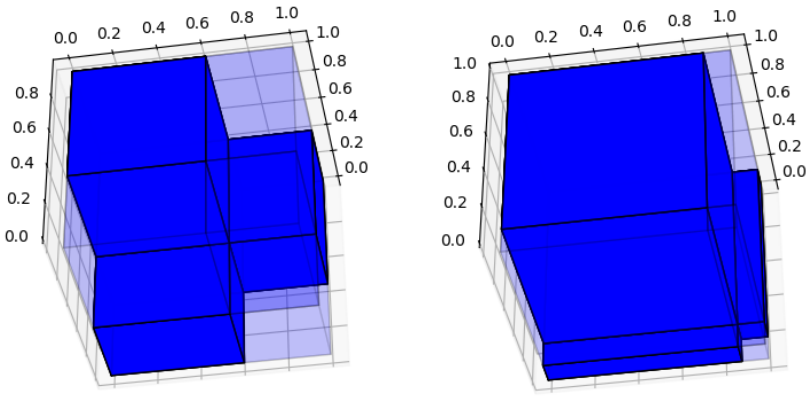

a) $V_f = 66\%$ b) $V_f = 95\%$

Fig. 2 Open-cell RUC.

Properties of solid Inconel 625 were used for the solid material, tabulated in Table 1. The mechanical properties of air were estimated as 7 orders of magnitude smaller than the mechanical properties of the solid material. The computed sintered material properties are plotted in Fig. 3 with respect to temperature. The figure shows that the yield strength and the stress for a given plastic strain decrease as the volume fraction decreases. A similar decrease in those properties can be seen as the temperature increases. All the material properties computed by MAC-GMC are tabulated in Table 4 in the appendix.

Table 1 Solid Inconel 625 properties as a function of temperature

Temperature °C	**20**	**200**	**400**	**700**	**900**
E GPa	204	193	181	161	145
υ	0.312	0.303	0.301	0.309	0.284
ρ $\frac{\text{kg}}{\text{m}^3}$	2700	2700	2700	2700	2700
k $\frac{\text{W}}{\text{m}^\circ\text{C}}$	9.8	12.5	15.3	19.8	23.3
C $\frac{\text{J}}{\text{kg}^\circ\text{C}}$	410	456	511	600	630
α $\frac{1}{^\circ\text{C}}$	12.6E-06	13.1E-6	13.6E-6	15.0E-6	1.60E-05
S_y MPa	618	610	491	501	195
$\varepsilon_{p,1}$	0.036	0.0782	0.0670	0.1024	0.0535
S_1 MPa	727	736	574	689	190
$\varepsilon_{p,2}$	.092	.2469	.1139	.1584	.2225
S_2 MPa	803	876	625	721	167
$\varepsilon_{p,3}$	.204	.3030	.2387	.4685	.4908
S_3 MPa	902	901	707	601	50

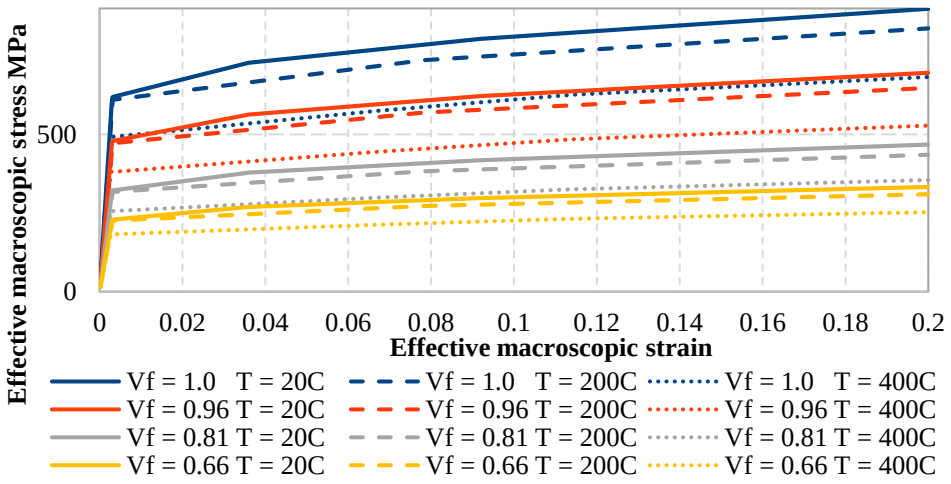

Fig. 3 Sintered material homogenized macroscopic stress-strain curve.

The powdered material properties were set equal to the sintered material properties, except for the modulus of elasticity, at a given temperature and volume fraction. The modulus was estimated to be an order of magnitude smaller than that of the sintered material for a given volume fraction at room temperature. As the temperature of the powder increases, the modulus of the powder was set to linearly increase, until 700°C, at which the modulus of the powder was made the same to that of the sintered material, at a given volume fraction. This was done to avoid strong C1 discontinuities in material properties and to avoid the strain-softening of the solid Inconel at high strains and temperatures, aiding in numerical convergence. It was assumed that this slow change in powder material properties to sintered material modulus would not adversely affect the results since the spatial gradient of temperature is extremely high near the laser. Thus, the temperature of the powder material is close to room temperature a small distance away from the laser, and at room temperature, the powder material has a low modulus. These powder material estimates are preliminary and used to establish the methodology. In the future, these properties can be measured and the sensitivity of the results to these properties investigated. Fig. 4 shows how this modulus changes with temperature and volume fraction. The solid line represents the linear interpolation used for temperatures not tabulated.

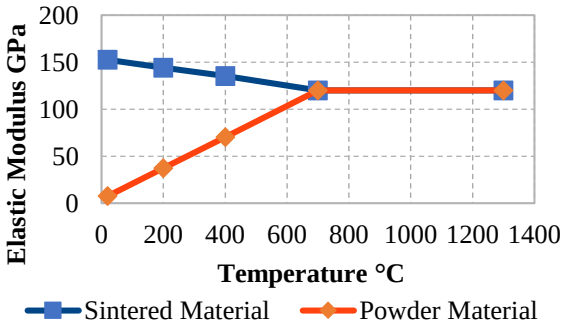

a) Elastic modulus vs. temperature at $V_f = 95\%$

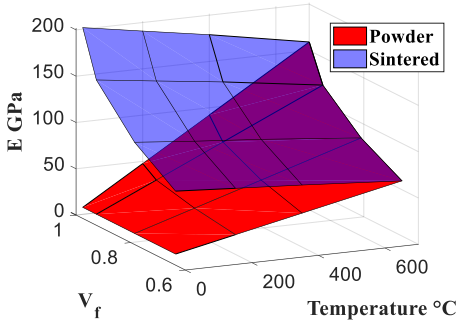

b) Elastic modulus vs. temperature vs. volume fraction

Fig. 4 Elastic modulus vs. temperature vs. volume fraction.

IV. Results

A. Boundary Conditions

The geometry used, along with the bed and mesh is shown in Fig. 5. The dimensions of the printed part are 12mm by 12mm by 3mm, while the bed is 9mm by 1.5mm by 18mm. The mesh used linear 8-noded bricks. The bottom of the bed was set to a constant temperature of 70°C, with no displacements. The elements in the mesh were approximately 1mm on each side. This allowed the heat flux from the laser beam (with a characteristic radius of 2.5mm) to be applied to several integration points during a time step. The layer thickness was taken as 1mm; thus, one element was used through the thickness of a layer.

The heat carried away by the powder surrounding the part was modeled as an effective convective heat transfer boundary condition, to avoid the computational cost of modeling the conductive heat flux into a physical region of excess powder. Here it was assumed that the unmodeled powder changed temperature from its maximum at the surface of the part to its steady-state, far-field temperature within 10mm. This gives an effective convective heat transfer coefficient of $h_{eff,powder} = k/L = 362\ \mathrm{W/m^2K}$, with an estimated conductive coefficient of $k_{powder} = 3.62\ \mathrm{W/mK}$ for the un-sintered powder. The powder thermal conductive coefficient k_{powder} was estimated from MAC-GMC with a volume fraction of 66%. A changing convective boundary condition was applied to the current topmost surface with a convection coefficient of $h_{air} = 100\ \mathrm{W/m^2K}$. A radiation boundary condition was also applied to the current topmost surface. The effective emissivity for the radiation was assumed to be 50%. The ambient temperature of the air was assumed to be 70°C, as well as the bed preheat temperature.

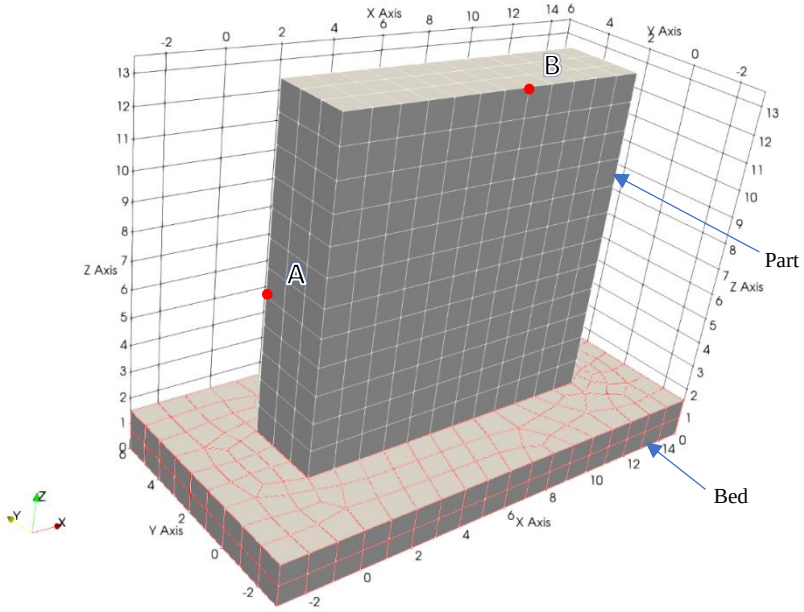

Fig. 5 Geometry and mesh used.

Fig. 6 shows the scanning pattern used. The laser path was discretized into time steps of 0.05 seconds for the FE simulation, as shown. The same path was used for all the layers. At a laser speed of 100mm/s (as shown in Table 2), a layer was scanned in about 5 seconds. With a dwell time of 1 second per layer, and 12 layers in the model the total simulated print time is 72 seconds. A dwell time of a second was enough to cool the part to ambient temperature in the simulation. Values used for the laser properties for Eq. (1) are listed in Table 2, adopted from Ref. [8].

Table 2 Laser parameters

η	r_0 mm	s mm	P W	v mm/s
1	2.5	1	2,250	100

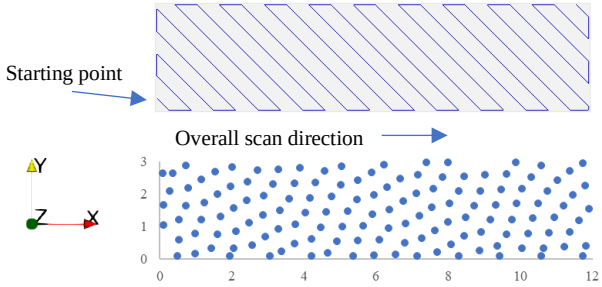

Fig. 6 Laser beam scanning path.

B. Evolving Porosity

Post-processing was accomplished with the open-source software ParaView. Fig. 7 shows the results of the simulation at the midpoint of part completion. Fig. 8 shows the results at the end process after cooling. Corresponding graphs are shown at the same scale.

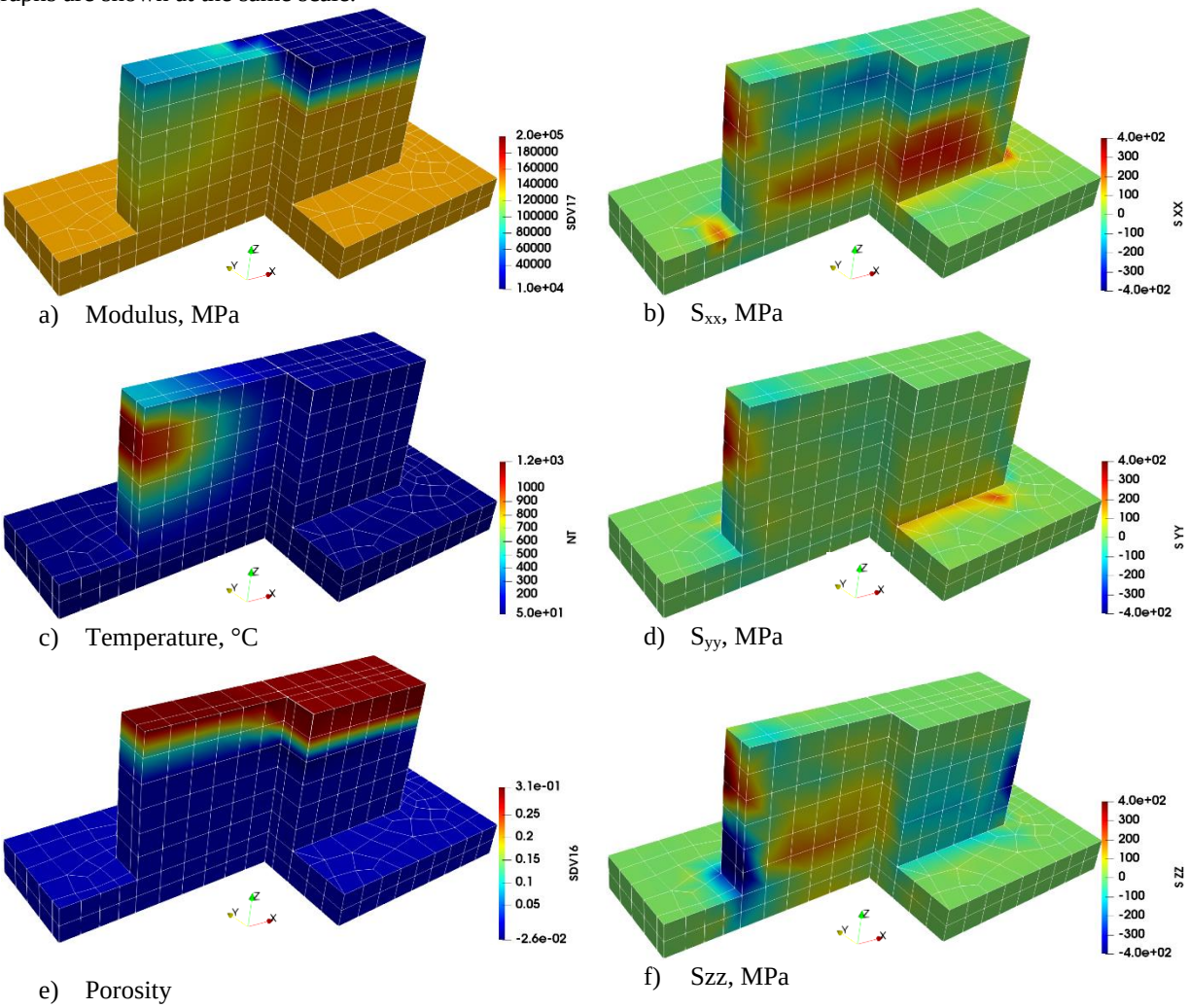

a) Modulus, MPa

b) S_{xx}, MPa

c) Temperature, °C

d) S_{yy}, MPa

e) Porosity

f) Szz, MPa

Fig. 7 Results at t = 31.5s, evolving porosity, no deformation shown.

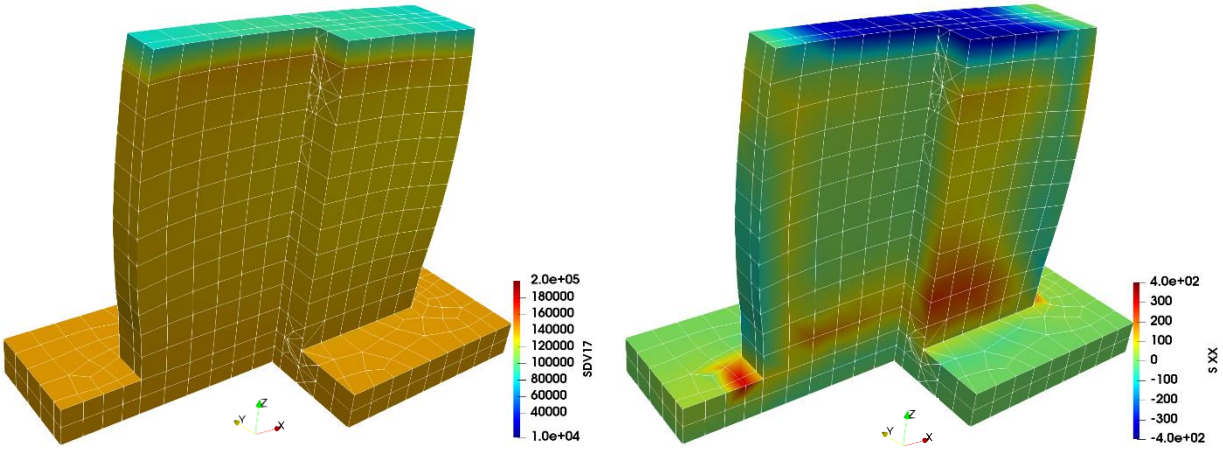

a) Modulus, MPa

b) S_{xx}, MPa

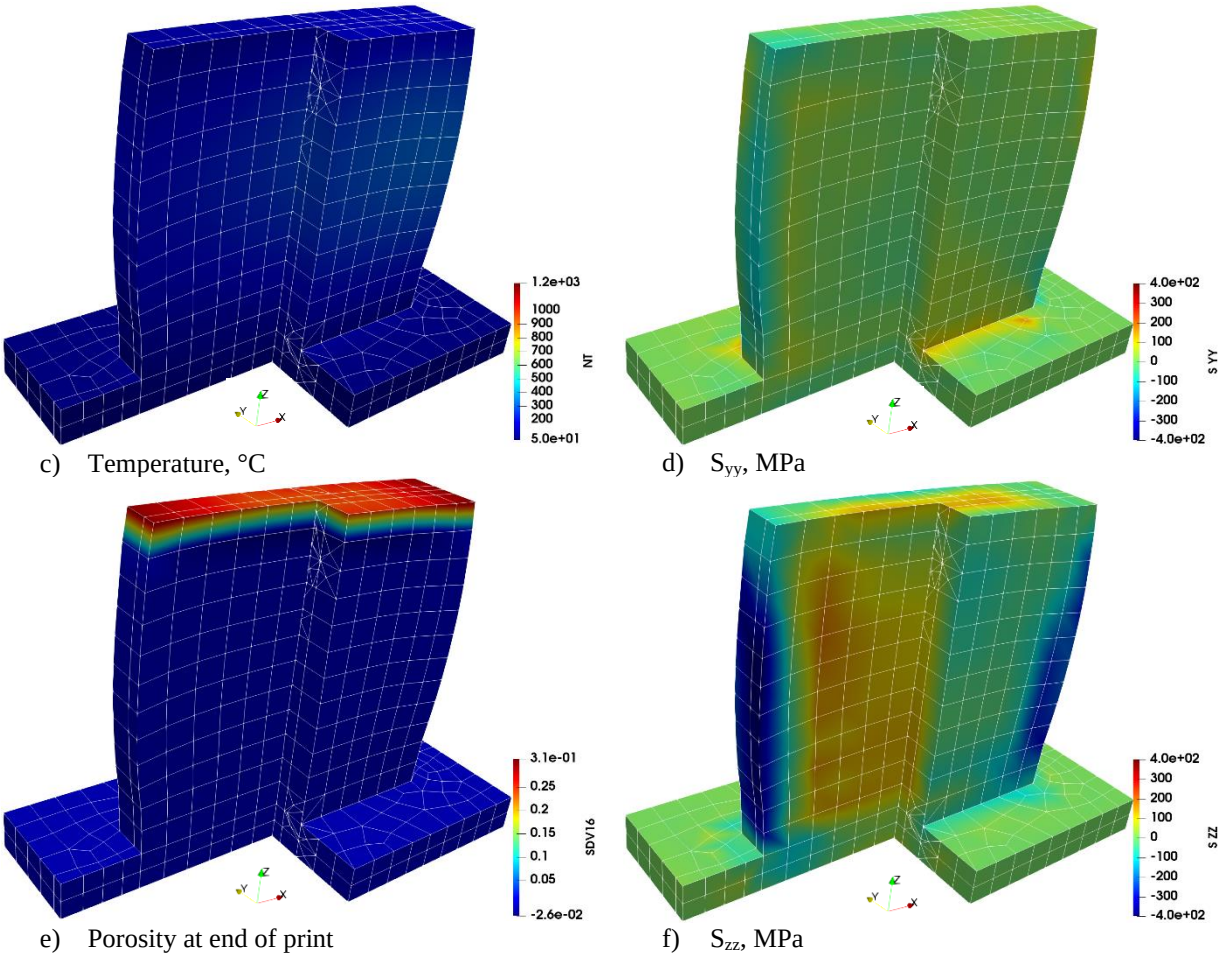

c) Temperature, °C

d) S_{yy}, MPa

e) Porosity at end of print

f) S_{zz}, MPa

Fig. 8 Results at the end of print, t = 72s, deformation magnified by 20x, evolving porosity.

Fig. 9 shows the estimated porosity evolution at a specific node in the model. The horizontal spacing of the data points indicates the time step sizes used by the solver. It shows that the predicted porosity decays from its initial value to its minimum value in approximately a second. The abrupt change in slope in the porosity vs. time plot corresponds with the position of the laser relative to the point in the material.

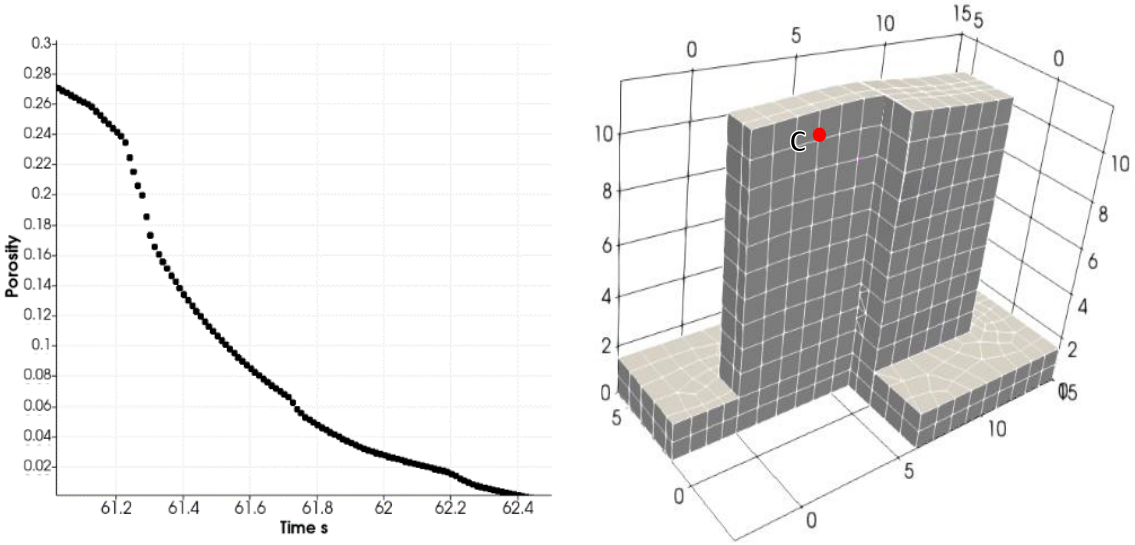

Fig. 9 Estimated porosity vs. time, at node point C.

The stresses in Fig. 7 and Fig. 8, subplots b, d, and f show that there are primarily compressive residual stresses on the outer surfaces while tensile towards the center. In addition, there are stress concentrations where the part meets the bed, as expected. In addition, the residual stresses in the z-direction are the greatest compared to the other two orthogonal stresses.

The porosity plot in Fig. 8 subplot e shows that there is still some porosity at the top surface. This could be due to the laser having passed over the top surface only once. The temperature plot in Fig. 7 subplot c, shows that the temperature is greater inside the part than at the top surface. This is may be explained by the convective and radiative boundary conditions on the surface combined with the volumetric heat flux. The temperature dependence of the elastic modulus can also be seen in Fig. 7 subplot a.

The deformation in Fig. 8, shows that the part swells at the center, with a small amount of deformation towards the top horizontal edges. This behavior also is seen during the simulation of the process, not just after part completion. In addition, the top four corners of the part tend to point in the positive z-direction.

C. Constant Porosity

A second model with a constant porosity of 10% was simulated for comparison. All other parameters including the mesh were kept the same as the previous evolving porosity simulation. Corresponding graphs are shown at the same scale as the previous simulation. The material properties were taken as only dependent on temperature and material state (powder or sintered). Fig. 10 and Fig. 11 shows the results of this simulation.

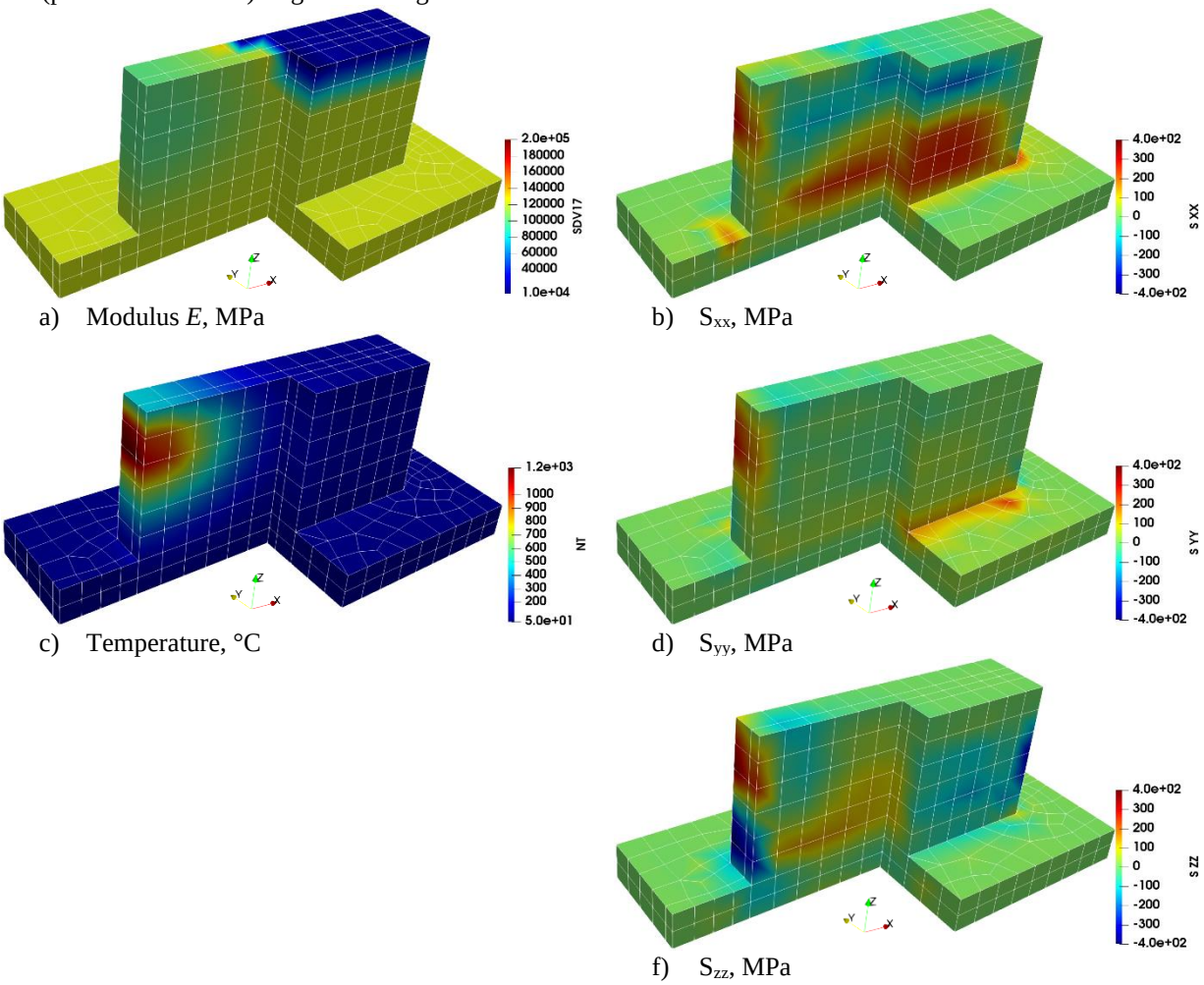

a) Modulus *E*, MPa

b) S_{xx}, MPa

c) Temperature, °C

d) S_{yy}, MPa

f) S_{zz}, MPa

Fig. 10 Results at t = 31.5s, constant porosity, no deformation shown.

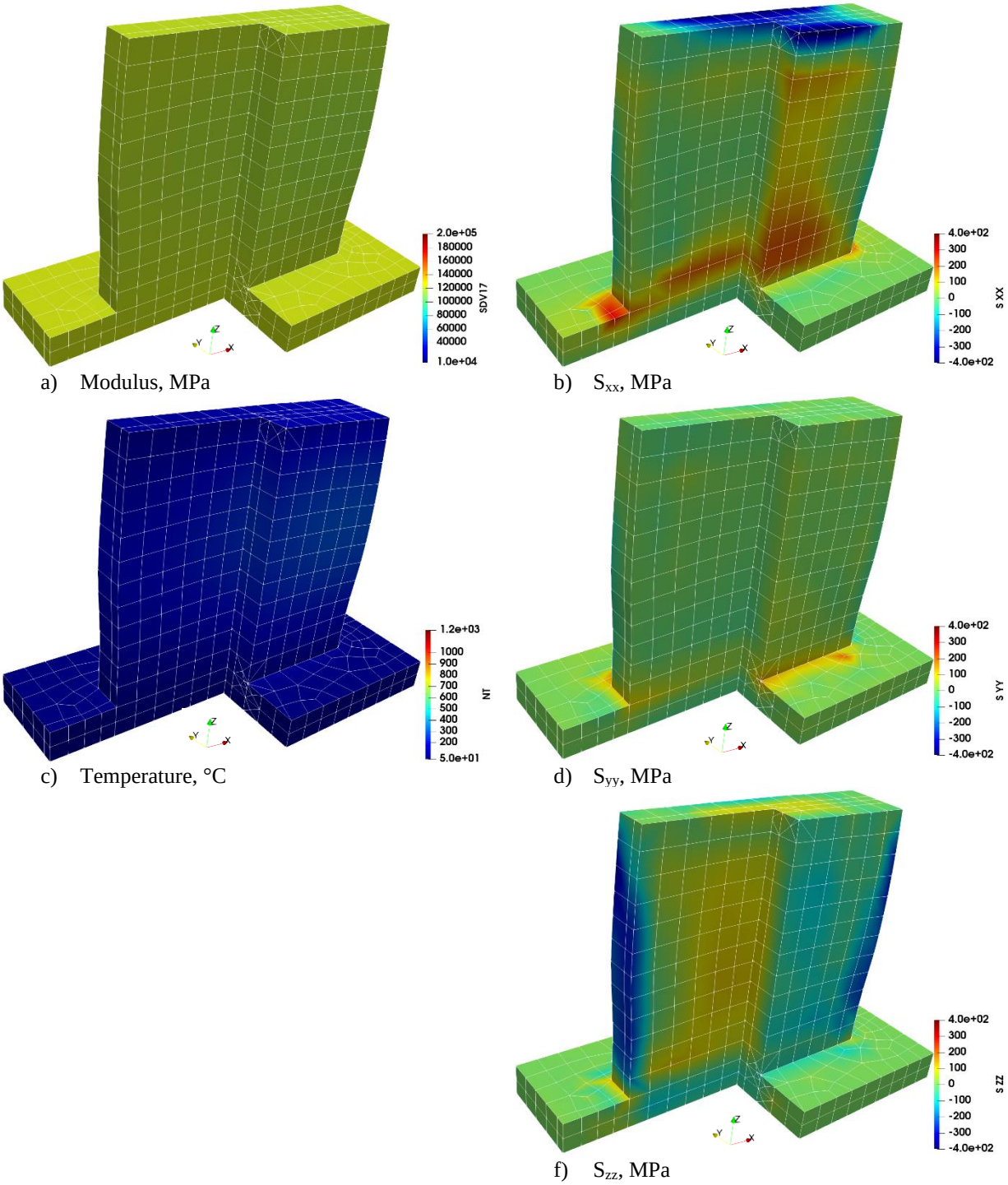

a) Modulus, MPa

b) S_{xx}, MPa

c) Temperature, °C

d) S_{yy}, MPa

f) S_{zz}, MPa

Fig. 11 Results at the end of print, t = 72s, deformation magnified by 20x, constant porosity.

The elastic modulus plot in Fig. 10 subplot a shows that compared to Fig. 8 subplot a, the change in the material's modulus from sintered to powder is more severe. This can adversely impact numerical convergence.

Fig. 10 and Fig. 11 show a similar trend in residual stresses at the end of the printing simulation and similar temperatures during the printing of the part. However, comparing subplots f (stresses in the z-direction), the evolving material model tends to show greater stresses in magnitude. Table 3 shows a comparison of residual stresses and distortions, at surface points A and B labeled on the geometry used in Fig. 5. Values with a greater magnitude are

highlighted for ease. The table shows that the differences in the models can be significant and that the evolving porosity model does not always give greater residual stresses or distortions.

Table 3 Residual stress and distortion comparison.

	Point A			Point B		
	Constant Porosity	Evolving Porosity	% increase in magnitude	Constant Porosity	Evolving Porosity	% increase in magnitude
S_{xx} MPa	-77	-55	-29%	-450	-364	-19%
S_{yy} MPa	-60	-16	-73%	-11	-1	-91%
S_{zz} MPa	-210	-246	17%	-38	-47	24%
U_{xx} mm	-.00894	-.016807	88%	.001025	.000541	-47%
U_{yy} mm	.000809	.006235	671%	.000174	-8.42e-5	-148%
U_{zz} mm	-.002287	-.013365	484%	.002095	.001269	-39%

V. Discussion

Comparing the stresses in subplots b, d, and f of Fig. 8 and Fig. 11 shows that modeling an evolving porosity results in higher overall residual stresses and larger deformations. The peak positive normal stress in the z-direction was calculated at 230MPa for the evolving porosity model, while the constant porosity model showed a peak positive stress of 145MPa. The evolving model had a peak displacement of 0.027mm while the constant model had a peak displacement of 0.016mm. Both models used the same laser parameters, boundary conditions, and mesh. This increase in deformation and residual stresses is likely due to the regions with high porosity having to carry the same load (due to thermal strains and constraints by the surrounding material) yet with a lower microscopic cross-sectional area. This reduced cross-sectional area can be seen by comparing the microscopic architectures in Fig. 2. The higher applied stresses may result in higher plastic strains, leading to higher residual stresses at part completion and higher part deformation.

A limitation of this work is that it does not include heat treatment effects subsequent to printing. In addition, to date, no experimental validation has been conducted on the presented work. Ongoing work includes the development of validation specimens. Furthermore, no mesh convergence has been conducted. A model with a refined mesh is currently in progress.

VI. Conclusion

It has been previously determined that the microstructure evolution and local temperature variation interact mutually [9]. This paper has used the densification coefficient K, coupled to a time-dependent thermal history, to yield an evolving volume fraction. The volume fraction is used with GMC to provide predictions of temperature and volume fraction dependent stress-strain and plasticity at the micro-scale. These material properties, used in a macro-scale finite element model, compute evolving volume fraction dependent residual stresses. In short, evolving volume fractions impact porosity and consequently impact the residual stresses and deformation.

Appendix

Table 4 Material properties computed by NASA's MAC/GMC from Table 1

Material	T °C	V_f	E MPa	υ	ρ $\frac{kg}{m^3}$	k $\frac{W}{m^{2\circ}C}$	C $\frac{J}{kg^{\circ}C}$	α $\frac{1}{^{\circ}C}$	S_y MPa	$\varepsilon_{p,1}$	S_1 MPa	$\varepsilon_{p,2}$	S_2 MPa
Powder	20	0.66	7,550	0.190	1,780	3.63	270	1.26E-5	324	0.032	270	0.088	298
		0.81	7,550	0.225	2,180	5.10	332	1.26E-5	327	0.032	380	0.088	419
		0.95	7,550	0.270	2,560	7.33	389	1.26E-5	469	0.032	546	0.088	602
		0.999	7,550	0.310	2,690	9.69	410	1.26E-5	621	0.032	722	0.088	796
	200	0.66	21,328	0.184	1,780	4.63	301	1.31E-5	227	0.032	273	0.088	273
		0.81	27,707	0.218	2,180	6.50	369	1.31E-5	317	0.075	382	0.244	455
		0.95	37,316	0.262	2,560	6.50	433	1.31E-5	456	0.075	550	0.244	655
		0.999	47,677	0.285	2,630	9.35	456	1.31E-5	540	0.075	652	0.244	776
	400	0.66	36,637	0.183	1,780	5.67	337	1.36E-5	182	0.111	232	0.236	262
		0.81	50,104	0.217	2,180	7.96	414	1.36E-5	256	0.111	325	0.236	368
		0.95	70,389	0.260	2,560	11.44	485	1.36E-5	367	0.111	468	0.236	529
		0.999	92,183	0.299	2,690	15.13	510	1.36E-5	486	0.111	618	0.236	700
	700	0.66	59,600	0.188	1,780	7.33	383	1.50E-5	186	0.099	255	0.155	267
		0.81	83,700	0.223	2,180	10.30	470	1.50E-5	261	0.099	359	0.155	375
		0.95	120,000	0.267	2,560	14.81	551	1.50E-5	375	0.099	516	0.155	540
		0.999	159,142	0.307	2,690	19.58	579	1.50E-5	496	0.099	682	0.155	714
Sintered	20	0.66	75,500	0.190	1,780	3.63	270	1.26E-5	324	0.032	270	0.088	298
		0.81	106,000	0.225	2,180	5.10	332	1.26E-5	327	0.032	380	0.088	419
		0.95	152,514	0.270	2,560	7.33	389	1.26E-5	469	0.032	546	0.088	602
		0.999	201,646	0.310	2,690	9.69	410	1.26E-5	621	0.032	722	0.088	796
	200	0.66	71,400	0.184	1,780	4.63	301	1.31E-5	227	0.032	273	0.088	273
		0.81	100,000	0.218	2,180	6.50	369	1.31E-5	317	0.075	382	0.244	455
		0.95	144,290	0.262	2,560	6.50	433	1.31E-5	456	0.075	550	0.244	655
		0.999	190,773	0.285	2,690	9.35	456	1.31E-5	540	0.075	652	0.244	776
	400	0.66	67,000	0.183	1,780	5.67	337	1.36E-5	182	0.111	232	0.236	262
		0.81	94,100	0.217	2,180	7.96	414	1.36E-5	256	0.111	325	0.236	368
		0.95	135,319	0.260	2,560	11.44	485	1.36E-5	367	0.111	468	0.2360	529
		0.999	178,911	0.299	2,690	15.13	510	1.36E-5	486	0.111	618	0.236	700
	700	0.66	59,600	0.188	1,780	7.33	383	1.50E-5	186	0.099	255	0.155	267
		0.81	83,700	0.223	2,180	10.30	470	1.50E-5	261	0.099	359	0.155	375
		0.95	120,000	0.267	2,560	14.81	551	1.50E-5	375	0.099	516	0.155	540
		0.999	159,142	0.307	2,690	19.58	579	1.50E-5	496	0.099	682	0.155	714

Acknowledgments

This work was supported by a NASA Space Technology Research Fellowship. The first author acknowledges the support of several NASA personnel including Brett Bednarcyk and Trenton Ricks for their support in using NASA's MAC/GMC.

References

[1] Mercelis, P., and Kruth, J. P., "Residual stresses in selective laser sintering and selective laser melting," *Rapid Prototyping Journal,* Vol. 12, No. 5, p. 254–265, 2006. doi: 10.1108/13552540610707013

[2] Xing, W., Ouyang, D., Li, N. and Liu, L, "Estimation of Residual Stress in Selective Laser Melting of a Zr-Based Amorphous Alloy," *Materials,* Vol. 11, No. 8, 2018. doi:10.3390/ma11081480

[3] Gobal, A., and Ravani, B., "Physical Modeling of Selective Laser Sintering Process," *Journal of Computing and Information Science in Engineering,* Vol. 17, No. 2, 2017. doi: 10.1115/1.4034473

[4] Aboudi, J., Arnold, S. M., and Bednarcyk, B. A., Micromechanics of composite materials: a generalized multiscale analysis approach, Butterworth-Heinemann, 2013. URL https://books.google.com/books?id=jKJ2VqSwu08C.

[5] Cheng, Bo, Shrestha, Subin, and Chou, Kevin, "Stress and deformation evaluations of scanning strategy effect in selective laser melting" *Additive Manufacturing*, Vol. 12, pp. 240-251, 2016. doi: 10.1016/j.addma.2016.05.007

[6] Kubiak, M., W. Piekarska, and R. Parkitny, "Theoretical study on thermal and structural phenomena in thin elements heated by a laser beam," *Archives of Mechanics*, Vol. 67, No. 1, pp. 3-24, 2015. URL http://search.ebscohost.com/login.aspx?direct=true&db=a9h&AN=100941759.

[7] Dhondt, G., and Wittig, K., "CalculixX: A Free Software Three-Dimensional Structural Finite Element Program," Web page, 1998. URL http://www.calculix.de/, accessed 2019-12-02.

[8] Jayanath, S., and A. Achuthan. "A Computationally Efficient Finite Element Framework to Simulate Additive Manufacturing Processes." *Journal of Manufacturing Science and Engineering*, Vol. 140, 2018. doi: 10.1115/1.4039092

[9] Yang, Y., Ragnvaldsen, O., Bai, Y., Yi, M., and Bai-Xiang, "3D non-isothermal phase-field simulation of microstructure evolution during selective laser sintering," *Computational Materials*, 2019. doi: 10.1038/s41524-019-0219-7